Restructuring of Palladium Nanoparticles during Oxidation by Molecular Oxygen

Oleg Usoltsev, Dragos Stoian, Alina Skorynina, Elizaveta Kozyr, Peter N. Njoroge, Riccardo Pellegrini, Elena Groppo, Jeroen A. van Bokhoven, and Aram Bugaev*

An interplay between Pd and PdO and their spatial distribution inside the particles are relevant for numerous catalytic reactions. Using in situ time-resolved X-ray absorption spectroscopy (XAS) supported by theoretical simulations, a mechanistic picture of the structural evolution of 2.3 nm palladium nanoparticles upon their exposure to molecular oxygen is provided. XAS analysis revealed the restructuring of the *fcc*-like palladium surface into the 4-coordinated structure of palladium oxide upon absorption of oxygen from the gas phase and formation of core@shell Pd@PdO structures. The reconstruction starts from the low-coordinated sites at the edges of palladium nanoparticles. Formation of the PdO shell does not affect the average Pd–Pd coordination numbers, since the decrease of the size of the metallic core is compensated by a more spherical shape of the oxidized nanoparticles due to a weaker interaction with the support. The metallic core is preserved below 200 °C even after continuous exposure to oxygen, with its size decreasing insignificantly upon increasing the temperature, while above 200 °C, bulk oxidation proceeds. The Pd–Pd distances in the metallic phase progressively decrease upon increasing the fraction of the Pd oxide due to the alignment of the cell parameters of the two phases.

1. Introduction

Palladium-based catalysts are extensively used for a wide range of industrially relevant oxidation reactions, such as the combustion of carbon monoxide and methane,[1–3] selective aerobic oxidation of alcohols,[4,5] and hydrocarbons,[6] synthesis of hydrogen peroxide,[7,8] oxidative cross-couplings.[9–13] The formation of palladium oxide during these reactions in both bulk samples and nanoparticles is not only the consequence of the presence of molecular oxygen in the reactant feed but can often be a prerequisite of the active catalytic phase.[2,14,15] For example, a group of Grunwaldt demonstrated that the active phase in Pd/ZrO₂ catalyst for methane combustion in car exhaust systems is palladium oxide, while high-temperature operation regime leads to sudden catalyst reduction accompanied with deactivation,[16] while for aerobic oxidation of benzyl alcohol over alumina supported palladium, the same group highlighted the better catalytic performance of metallic phase compared to palladium oxide.[4] In contrast, Pd(II) state proved active and stable species in our recent study on aerobic oxidation of 2-propanol.[5]

Pioneering works based on indirect approaches (e.g., estimation of oxygen consumption)[17–20] paved the way for understanding the mechanism by which bulk Pd samples and Pd nanoparticles are oxidized by molecular oxygen, and the reverse (i.e., palladium oxide is reduced by hydrogen, carbon monoxide, and other gasses), but did not allow one to reveal whether oxide, metallic or a mixed phase was formed under certain reaction conditions. This was made possible much later,

O. Usoltsev, A. Skorynina
ALBA Synchrotron
Cerdanyola del Valles, Barcelona 08290, Spain
D. Stoian
The Swiss-Norwegian Beamlines (SNBL) at ESRF
BP 220, Grenoble 38043, France
E. Kozyr, E. Groppo
Department of Chemistry, INSTM and NIS Centre
University of Torino
via Quarello 15A, Turin 10125, Italy

P. N. Njoroge
Department of Chemistry
University of Oslo
Sem Saelandsvei 26, Oslo 0315, Norway
R. Pellegrini
Chimet S.p.A. – Catalyst Division
Via di Pescaiola 74, Viciomaggio Arezzo 52041, Italy
J. A. van Bokhoven, A. Bugaev
Paul Scherrer Institute
Villigen 5232, Switzerland
E-mail: aram.bugaev@psi.ch
J. A. van Bokhoven
Institute for Chemical and Bioengineering
ETH Zurich
Vladimir-Prelog-Weg 1, Zurich 8093, Switzerland

**ADVANCED
SCIENCE NEWS**

www.advancedsciencenews.com

NANO · MICRO

small

www.small-journal.com

by the advent of *operando* spectroscopies, including X-ray photoelectron spectroscopy[21] and X-ray absorption spectroscopy (XAS),[22–24] which rapidly became one of the most powerful methods to determine the average oxidation state and the local structure of metal sites under reaction certain conditions reaction, allowing one to establish structure-activity correlations. This was successfully demonstrated in recent studies from different groups (see, e.g.,),[14,15,25–29] and even in the liquid phase as reported by Fovanna et al.[30] An oscillatory behavior between the metallic Pd and palladium oxide phases was detected by time-resolved XAS on a Pd/Al$_2$O$_3$ catalyst during methane oxidation. These data, coupled with information on the catalytic activity, evidenced the importance of the palladium oxide phase and the negative effect of auto-reduction phenomena on the catalytic properties.[31] In agreement with these conclusions, the stabilization of palladium oxide clusters was shown to improve methane oxidation activity.[32]

Apart from determining the average oxidation state and first-shell coordination of palladium under reaction conditions, a systematic XAS study can also reveal the spatial distribution of the Pd phases (e.g., core-shell structures),[33,34] which is relevant to catalytic properties.[15,21] However, the extraction of such detailed information from XAS data is not a trivial task. In this context, we have recently applied in situ and *operando* XAS complemented by advanced analysis of both extended (EXAFS) and near-edge (XANES) regions to reveal subsurface and bulk palladium hydrides,[34–39] surface and bulk carbides,[22,39–46] and oxides.[15,47] In particular, we unambiguously demonstrated how the combined analysis of EXAFS and XANES regions, coupled with complementary techniques, can discriminate between the bulk and surface structure of nanoparticles.

Herein, we extend our investigation presenting a systematic time-resolved XAS study of well-defined supported Pd nanoparticles during their oxidation upon exposure to molecular oxygen and successive reduction by hydrogen. The XANES region was used to estimate the averaged Pd(II)/Pd(0) ratio. A core@shell Pd@PdO model was applied to fit EXAFS data, providing information on the evolution of the core/shell ratio and structural parameters of Pd–Pd and Pd–O contributions. The experimental data were complemented by density functional theory (DFT) calculations of Pd and PdO phases and molecular dynamics simulations of the oxidation process over ns timescales using ReaxFF potentials.

2. Results and Discussion

2.1. Analysis of the XANES Data: Surface versus Bulk Oxidation

Figure 1 shows the XANES spectra of the fully reduced Pd(0)/Al$_2$O$_3$ catalyst before (black) and after (red) exposure to 20% O$_2$/He feed (evolution is shown in gray) at eight selected temperatures in the 50–400 °C range. The spectra of the metallic Pd foil and bulk palladium oxide are also reported as references (black and red dashed curves, respectively). At all temperatures, as soon as the fully reduced Pd(0)/Al$_2$O$_3$ catalyst gets in contact with O$_2$, its XANES spectrum rapidly changes and the spectral features characteristic of palladium oxide appear, indicating the partial oxidation of Pd(0) to Pd(II). For temperatures below

200 °C, although the initial changes are immediate, the final spectrum (collected after 40–70 min in O$_2$) is still different from that of the bulk palladium oxide, suggesting that the oxidation involves only a fraction of the Pd(0) nanoparticles. Above 200 °C, instead, the final spectrum is very similar to that of bulk palladium oxide. Notably, at each investigated temperature, reduction in H$_2$ immediately (below the time achieved resolution of 10 s per spectrum) brings the system back to the Pd(0) state (gray background).

These time-resolved data were subjected to a PCA analysis, which revealed only two components in the whole XANES dataset (i.e., Pd(0) metallic phase and Pd(II) oxide, Figure S1,Supporting Information), except for the data collected at 50 °C, where an additional component was related to the presence of palladium hydride during the reduction step. As reported earlier,[22–24] the XANES shaping of the hydride component is very similar to that of the pure metallic one, which is due to the fact that PdH$_x$ structures preserve the *fcc*-like orientation of Pd atoms and Pd(0) oxidation state. However, the increase of the Pd–Pd distances results in a slight shift of the resonances above the edge toward lower energies. Nevertheless, such spectra do not share common features with the characteristic XANES spectrum of PdO with its increased white line and completely different fingerprint of maxima and minima (See, e.g., dashed red lines in Figure 1. Therefore, further MCR analysis was performed using only two components. The results of the MCR analysis are summarized in **Figure 2**, which reports the fraction of Pd(II) in the Pd/Al$_2$O$_3$ catalyst as a function of time for all the investigated temperatures. Below 200 °C, a rapid increase of the Pd(II) fraction is observed as soon as O$_2$ is present in the feed, accounting for ≈30%–40% of the total, followed by a plateau with a very slow increase over an hour time-scale. The maximum amount of Pd(II) fraction is ≈0.3 at 50 °C and it increases to ≈ 0.5 at 180 °C. Starting from 220 °C, another behavior is observed, resulting in further growth of Pd(II) with kinetics strongly dependent on temperature. At 220 and 260 °C, an initial and rapid appearance of a Pd(II) fraction (≈30% of the total) is observed, followed by a slow growth at longer times. The plateau is reached after more than one hour, and the final Pd(II) fractions are as high as ca. 0.8 and 0.9, for 220 and 260 °C respectively. At higher temperatures, the initial fraction of Pd(II) is much larger and the plateau is reached almost immediately, with final Pd(II) fractions close to 100%. Considering the nanometric dimensions of the particles, the rapid growth of the Pd(II) fraction at the beginning of each oxidation step is explained in terms of surface oxidation, which accounts for a Pd(II) fraction of ≈30% of the total. Bulk oxidation starts above 200 °C and proceeds faster at higher temperatures.

The data for Pd(II) formation as a function of time were fitted with an exponential function of the type $f(x) = A_s - A_0 e^{-k(t-t_0)}$ (Figure S2, Supporting Information), where A_s corresponds to the final Pd(II) values at each temperature, A_0 is the fraction of metallic phase at $t = t_0$, and k is the rate constant of the oxidation process. These values are shown in **Figure 3a**, which highlights that 200 °C is the border between surface and bulk oxidation: below 200 °C, only the surface of the Pd(0) nanoparticles is oxidized, while above 200 °C oxidation of the Pd(0) core takes place. Moreover, the three Pd(II) formation curves collected at 220, 260, and 300 °C were used to evaluate the activation energy of bulk oxidation (E_A) through the Arrhenius plot reported in Figure 3b, which
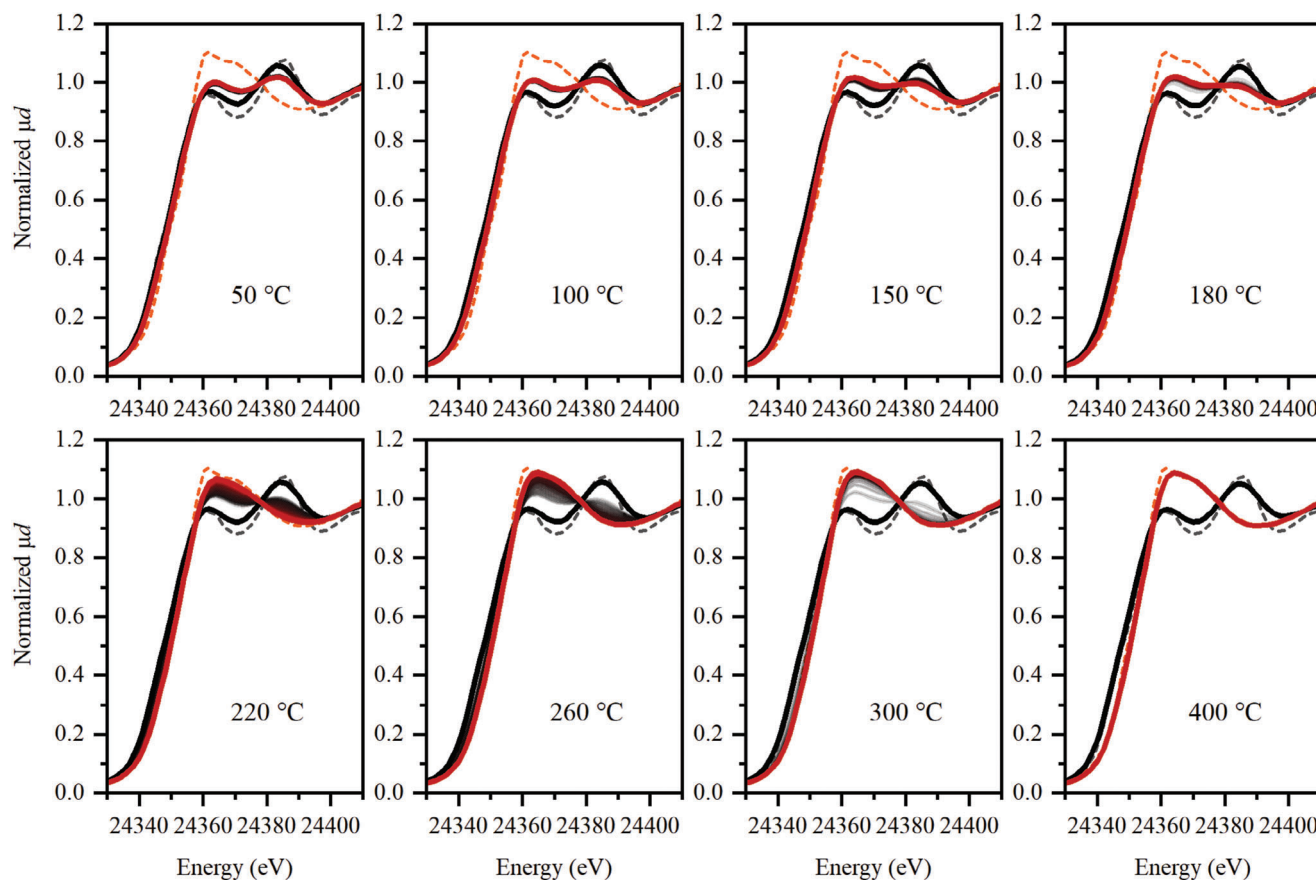
Figure 1. Evolution of the normalized Pd K-edge XANES spectra for Pd/Al$_2$O$_3$ sample (black) during oxidation at different temperatures (gray sequence up to red). The spectra of bulk palladium foil and palladium oxide are shown for comparison (grey and orange dashed spectra, respectively).

shows the $\ln(k)$ versus $1/T$. The data collected at temperatures below 200 °C were not considered since only surface oxidation took place. Those collected at the highest temperature were also excluded from the analysis since the oxidation occurs faster than the experimental time resolution. The slope of the linear regression gives $E_A = 21.5 \pm 2.5$ kJ mol^{-1}, which is in good agreement with previous reports (e.g., for zirconia-supported palladium with a much lower dispersion, 4%, $E_A = 24$ kJ mol^{-1}).[18]

2.2. Analysis of the EXAFS data: Evolution of Structural Parameters

To get a deeper insight into the reconstruction of the palladium nanoparticles upon oxidation, the time-resolved and steady-state EXAFS data were analyzed. At the first stage, we have compared the Fourier-transformed (FT) spectrum of the fully oxidized Pd(II)/Al$_2$O$_3$ catalyst to that of bulk PdO (Figure S3, Supporting Information) and that of the fully reduced Pd(0)/Al$_2$O$_3$ catalyst at room temperature with Pd foil (Figure S4, Supporting Information). Notably, the first shell Pd–O contribution (1–2 Å region, phase-uncorrected, (Figure S3a, Supporting Information) in Pd(II)/Al$_2$O$_3$ is similar to that in bulk PdO, while the higher shell Pd–Pd contribution ($\approx$3 Å, phase-uncorrected) is significantly reduced in the catalyst due to the nanometric dimensions

of the nanoparticles. The former means that, on average, all Pd atoms in the oxidized nanoparticles, including those at the surface, are 4-coordinated with oxygen atoms, making the first-shell Pd–O peak intensity independent of the particle size. The fact was also confirmed numerically by first-shell fitting of the experimental data. In contrast, the first shell Pd-Pd peak for the fully reduced Pd(0)/Al$_2$O$_3$ sample (Figure S3b, Supporting Information) is remarkably lower than that of metallic Pd, as expected for Pd nanoparticles, since the Pd atoms at the surface have a much lower coordination number than those in the bulk. The average coordination number as determined by a first shell EXAFS fit is 9.8 ± 0.4, in agreement with previously reported data.[33,42,44]

Figure 4 shows the k^2-weighted |FT| spectra of Pd/Al$_2$O$_3$ before (black) and after (red) oxidation at the eight different temperatures investigated. At each temperature, even below 200 °C, when only surface oxidation was hypothesized, the first shell Pd–O contribution grows at the expense of the first shell metallic Pd–Pd contribution. This indicates that upon oxidation, a fraction of the Pd atoms is converted from a fcc-like metallic structure into the 4-coordinated structure of PdO. It is worth noticing that the intensity of the metallic Pd–Pd contribution is progressively lower upon increasing the temperature, even though the Pd–Pd coordination number does not change (*vide infra*). This is a consequence of the increase in the dynamic Debye-Waller factor at high temperatures.
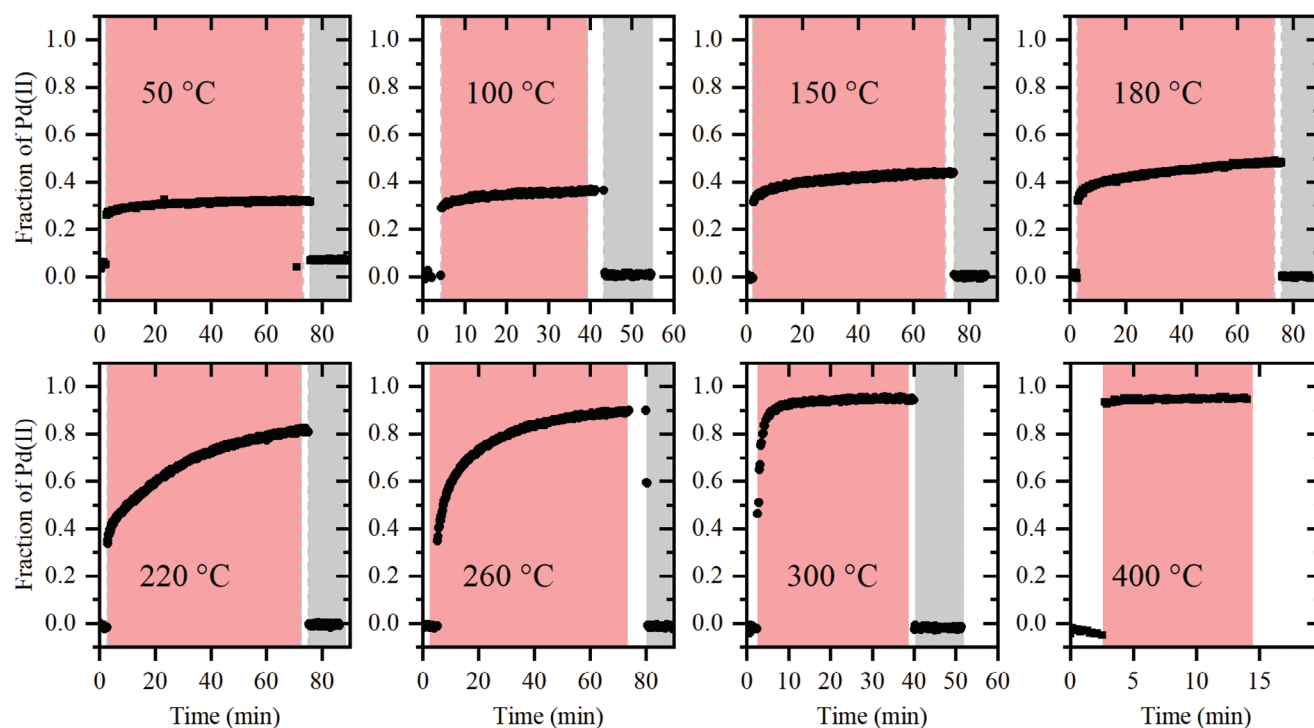
ADVANCED
SCIENCE NEWS
www.advancedsciencenews.com

NANO · MICRO
small
www.small-journal.com

Figure 2. Fraction of Pd(II) in the Pd/Al$_2$O$_3$ catalyst as a function of time, as determined by MCR analysis of the XANES spectra collected during oxidation in O$_2$ (red background) and successive reduction in H$_2$ (grey background) at different temperatures. Data reported on a white background have been collected under inert atmosphere.
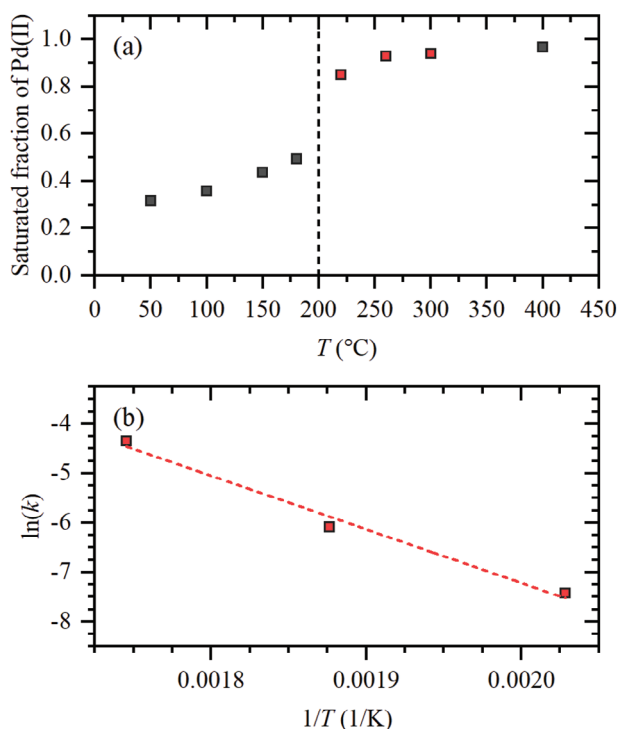

Figure 3. a) The saturated values of Pd(II) fraction as a function of the oxidation temperature and b) Arrhenius plot, i.e., the rate of Pd(0) bulk oxidation to Pd(II) as a function of the inverse temperature, as determined by exponentially fitting the Pd(II) formation curves reported in Figure 2.

The high quality of the time-resolved EXAFS data allowed us to fit every individual spectrum from the whole sequence collected during the oxidation at each temperature using the following procedure: i) the fit was performed with two contributions, Pd–O and Pd–Pd weighted for the relative fractions of α and (1–α), respectively; ii) interatomic distances, zero energy shift and Debye-Waller parameter were independently varied for each contribution; iii) coordination number for the Pd–Pd contribution was varied, while for Pd–O it was fixed to 4. This model neglects the second coordination shell (Pd–Pd) of the oxide phase, but its contribution is i) much weaker than Pd–Pd contribution from the metallic palladium (e.g., compare the absolute intensities of FT-EXAFS peaks in dotted lines in Figure S3 (Supporting Information), parts a and b) and ii) the amount of Pd oxide phase is high only at elevated temperatures, where the higher shell Pd–Pd contribution is significantly suppressed. Also, the Pd–Pd contribution of the oxide phase is located at a higher R-region compared to the metallic palladium (3.0 vs. 2.5 Å, phase-uncorrected). For pure metallic particles, the Pd–O contribution was removed from the fit, since its inclusion led to unreasonable values associated with this path; similarly, for mainly oxidic particles the Pd–Pd contribution was removed.

Figure 5 reports the fraction of oxide phase, α, as a function of time (black) together with the coordination numbers of the metallic Pd–Pd contribution (blue) as obtained from this analysis, while the fit results for other structural parameters are shown in Figures S4-S5 of the Supporting Information. The kinetics of the palladium oxide phase formation, α, are in perfect agreement with those independently obtained from XANES (Figure 2).
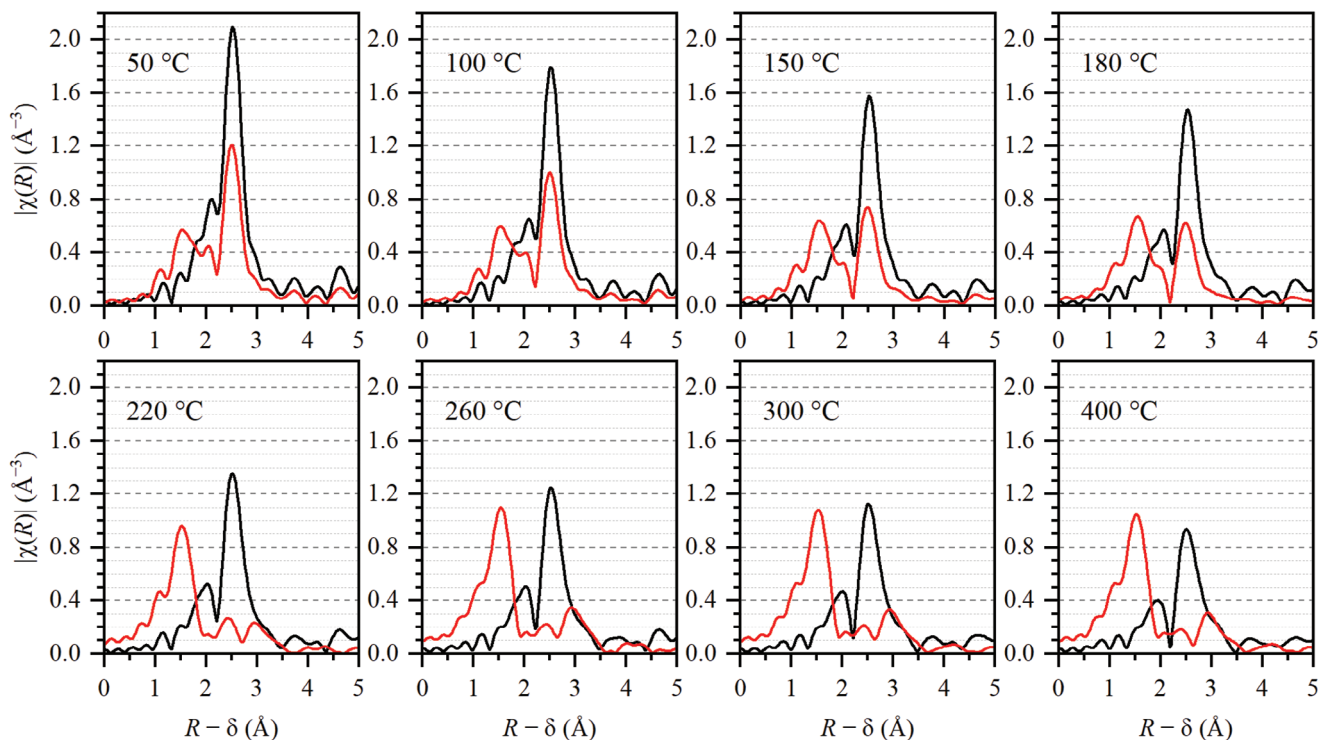
ADVANCED
SCIENCE NEWS

www.advancedsciencenews.com

NANO · MICRO

small

www.small-journal.com

Figure 4. The amplitude of the k^2-weighted FT of the EXAFS data (phase uncorrected) for the Pd/Al$_2$O$_3$ sample before (black) and after (red) oxidation at different temperatures.
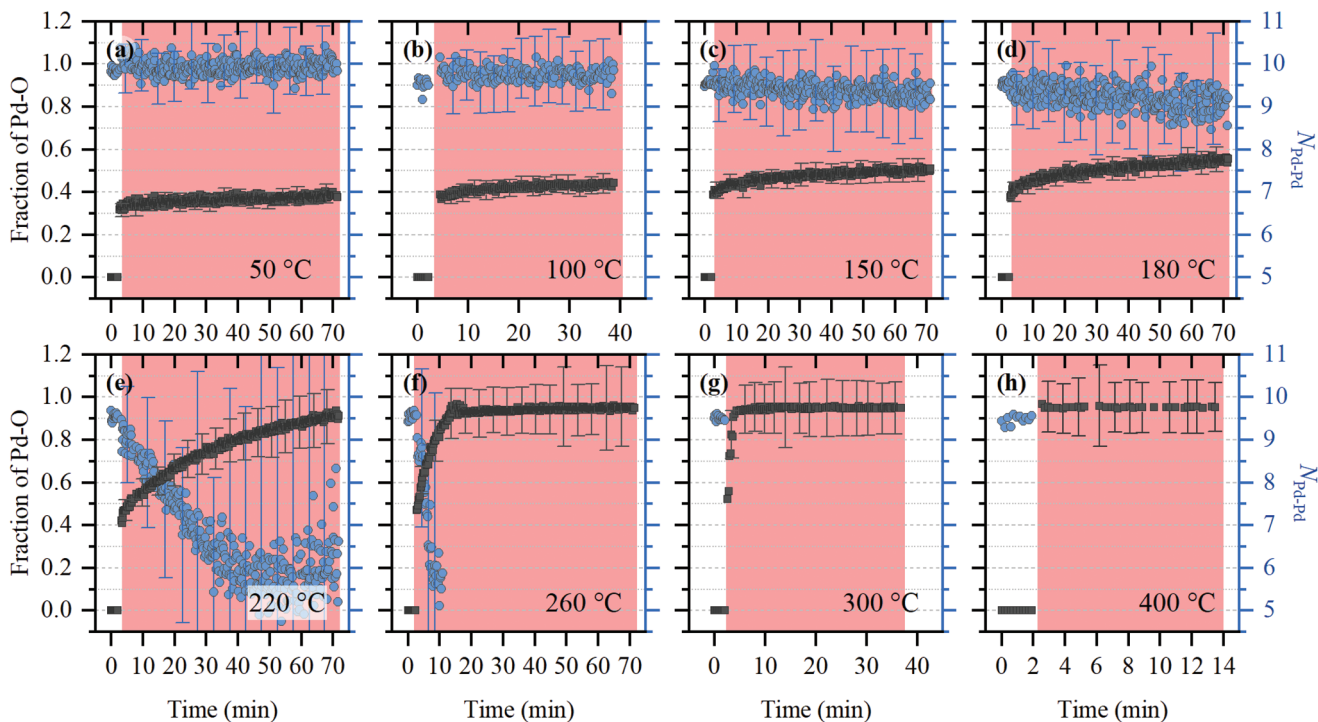

Figure 5. Fraction of PdO phase, α, (black squares, left ordinate axis) and the average Pd–Pd coordination number, $N_{\text{Pd-Pd}}$, (blue circles, right ordinate axis) obtained by fitting the time-resolved EXAFS data for Pd/Al$_2$O$_3$ during oxidation in O$_2$ (red background) at different temperatures from 50 to 400 °C (a–h).
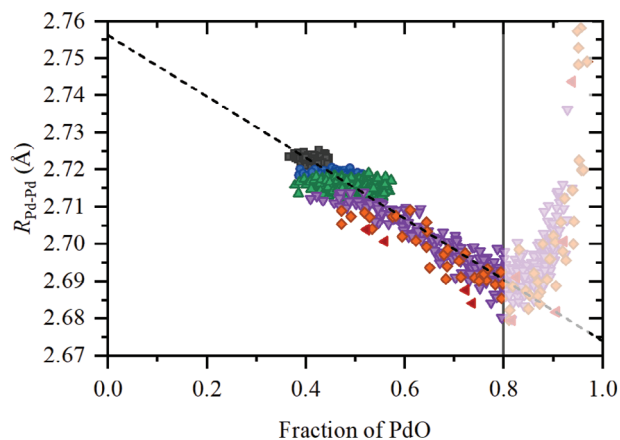
Figure 6. The first shell Pd–Pd interatomic distance in the metallic part of the nanoparticles as a function of the oxide phase fraction (α) at 100 (black), 150 (blue) 180 (green), 220 (purple) 300 (red) and 400 (dark red) °C. The dashed line is obtained by fitting the data up to $\alpha = 0.8$. The region with a white shadow suffers from fit instability.

Below 200 °C, the average Pd–Pd coordination numbers, N_{Pd-Pd}, are close to those obtained for metallic particles and slightly, but systematically decrease as a function of time upon increasing the temperature. Above 200 °C, N_{Pd-Pd} decreases with time, which happens faster at higher temperatures. This gives a solid proof that the metallic core of the particles shrinks while the oxidic shells grow inside their bulk.

Another particular behavior was observed for the average Pd–Pd interatomic distances (**Figure 6**; Figure S4, Supporting Information), whose values decrease from ≈2.74 Å for the Pd(0)/Al$_2$O$_3$ to 2.71–2.72 Å, and keep on decreasing down to 2.69 Å upon formation of bulk oxide phase. This behavior was observed for all temperatures but is most evident at 220 °C, where the bulk oxide formation is the slowest. It should be noted, that although the standard error in the determination of Pd–Pd distances is close to 0.01 Å for pure Pd(0)/Al$_2$O$_3$ and it increases with decreasing of the metallic phase fraction, the relative change in the interatomic distances can be determined by EXAFS with much better precision.[65] This is also confirmed by a very small deviation from a clear linear trend in R_{Pd-Pd}, observed in the Figure 6 up to PdO fractions of ≈0.8. For a higher fraction of PdO, a sudden increase in R_{Pd-Pd} might be caused by a higher instability of the fitting parameters of the metallic phase, whose fraction becomes negligible. This is also confirmed by a significant increase of absolute errors and unphysical changes of ΔE_0 parameter of metallic Pd–Pd path or PdO fractions > 0.8 (see data, e.g., for 220 and 260 °C in Figure S6, Supporting Information). Alternatively, this can be affected by the second shell Pd–Pd contribution of the PdO phase.

2.3. Interpretation of EXAFS Data: Oxidation of Low Coordinated Sites, Reshaping

In the previous section, the fit of the EXAFS data collected at temperatures below 200 °C revealed that the formation of the surface palladium oxide does not lead to a significant reduction of the average coordination numbers in the metallic phase (N_{Pd-Pd}),

which remains close to that of the pristine metallic nanoparticles in absence of O$_2$. Only when bulk PdO is formed, at temperatures above 200 °C, the N_{Pd-Pd} drastically decreases. This result is unexpected, since the formation of the surface oxide should reduce the size of the metallic core and lead to smaller coordination numbers. Another confirmation of the fact that this is not happening comes from the visual analysis of higher shell signals in FT-EXAFS data. In general, when the particle size decreases, the intensity of higher shell peaks decreases faster than that of the first shell peak, as can be seen by comparing the spectra of bulk Pd and Pd(0)/Al$_2$O$_3$ (Figure S3b, Supporting Information). However, after the formation of surface oxide, all higher-shell peaks are reduced proportionally to the first shell one (Figure 4), which can be caused by a lower fraction of metallic palladium, but not the smaller metallic core of the particles.

The first hypothesis that can explain such behavior is the reshaping of the particles to a more spherical form that compensates for the lowering of the coordination numbers due to the formation of the oxide shell. This hypothesis was supported by weaker metal-support interaction observed for smaller nanoparticles supported on P4VP (**Figure 7**). Being stable in both O$_2$ and H$_2$ at temperatures below 180 °C, exposure to oxygen at 220 °C led to the spontaneous growth of nanoparticles with the increase of the average coordination number from 6, for activated fresh reduced Pd/P4VP to 10. This is also evidenced in Figure S7 (Supporting Information), by the growing Pd-Pd contribution after the atmosphere was switched from He to O$_2$. A similar effect was observed earlier for this type of sample in the process of alcohol oxidation,[15] and for bigger particles at higher temperatures during methane combustion.[66] Thus, under oxygen, the interaction of Pd particles with the support becomes weaker, which can lead to reshaping or sintering that affects coordination numbers. This goes in line with the known fact that the surface energy of palladium oxide is lower than that of metallic palladium. Therefore, the latter should maximize its interaction with the support.

An additional explanation of the constant coordination numbers is the involvement of low-coordinated surface sites in the oxidation process. Such atoms can form bonds with oxygens, but this may not result in a decrease in the average Pd–Pd coordination numbers. Molecular dynamics (MD) simulations with ReaxFF potentials, that account for the creation and cleavage of chemical bonds, were performed to mimic this process. A series of MD simulations were run on an unsupported Pd$_{561}$ cluster having a cuboctahedral morphology, in the presence of O$_2$ at 0, 200, and 400 °C (273, 473, and 673 K). The snapshots of the oxidation process at the three temperatures as a function of time are shown in **Figure 8**. At all temperatures, the oxidation process starts from the low-coordinated Pd-sites located on the edges of the nanoparticle. Therefore, the oxide fraction affects those Pd atoms whose contribution is minimal to the average coordination number, which agrees with EXAFS data. While upon the growth of the bulk oxide, the size of the metallic core shrinks and the average metal-metal coordination numbers decrease as evidenced by EXAFS in Figure 5e,f. In a real experiment, one should also consider the size distribution of nanoparticles. Nanoparticles with smaller sizes and a higher number of low-coordinated sites are more prone to oxidation giving less effect on the reduction
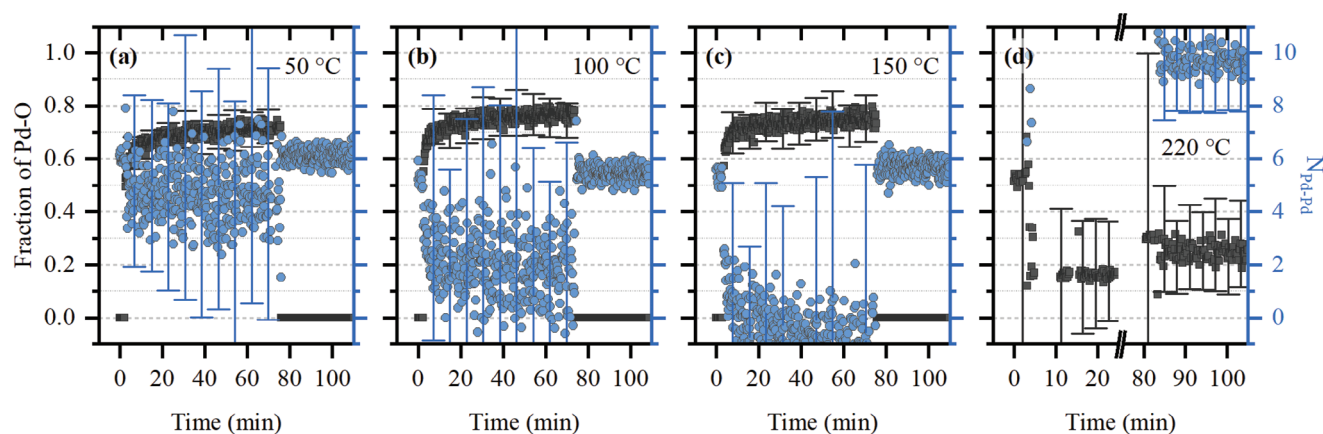
ADVANCED
SCIENCE NEWS
www.advancedsciencenews.com

NANO · MICRO
small
www.small-journal.com

Figure 7. Fraction of PdO phase, α, (black squares, left ordinate axis) and the average Pd–Pd coordination number, N_{Pd-Pd}, (blue circles, right ordinate axis) obtained by fitting the time-resolved EXAFS data for Pd/P4VP during oxidation at different temperatures from 50 to 220 °C a–d).

of EXAFS-derived Pd–Pd coordination numbers. In addition, the simulation showed that among the available nanoparticle's surfaces, the Pd(100) ones are preferentially oxidized (square-shaped faces) compared to Pd(111) (triangle-shaped phases), which is consistent with experimental reports.[67]

The final effect discussed in this section is the shortening of Pd–Pd distances in the metallic phase observed upon oxidation. As can be seen from Figure 6 and Figure S4 (Supporting Information), the Pd–Pd interatomic distances get shorter upon the

formation of an oxide layer, and further reduce upon formation of bulk oxide. Based on the previous result, we considered the formation of ($\sqrt{5}\times\sqrt{5}$)R27° PdO(101) layer on the Pd(100) surface. **Figure 9** shows the energy profiles of the metallic and oxide phases as a function of the cell parameter which is substituted in the abscissa axis by the equivalent first-shell interatomic distance in the metallic phase. The equilibrium cell parameter for the metallic palladium surface corresponds to the Pd–Pd distance of 2.728 Å, which is slightly lower than the experimental
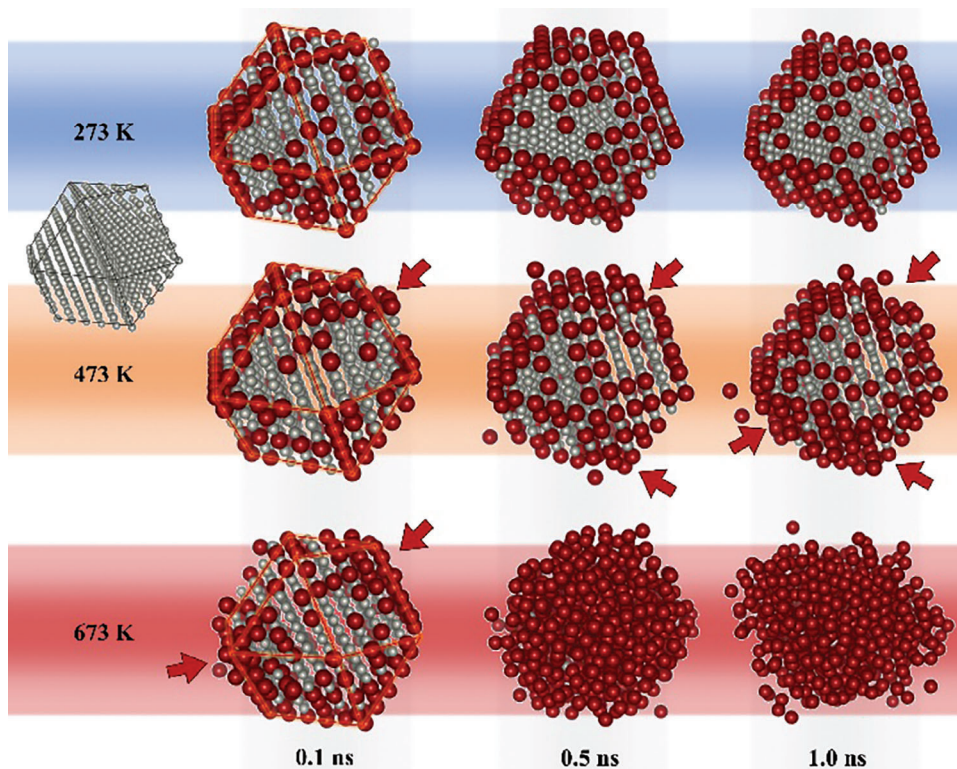

Figure 8. Snapshots from ReaxFF molecular dynamics simulations for un unsupported Pd_{561} particle in O_2 atmosphere at after 0.1, 0.5, and 1.0 ns at three different temperatures. Grey and red atoms correspond to metallic and oxidized Pd atoms, respectively. Red arrows highlight the regions where the oxidation of subsurface Pd atoms occurs. Black and red lines highlight the edges of the particles in the initial state and after 0.1 ns.
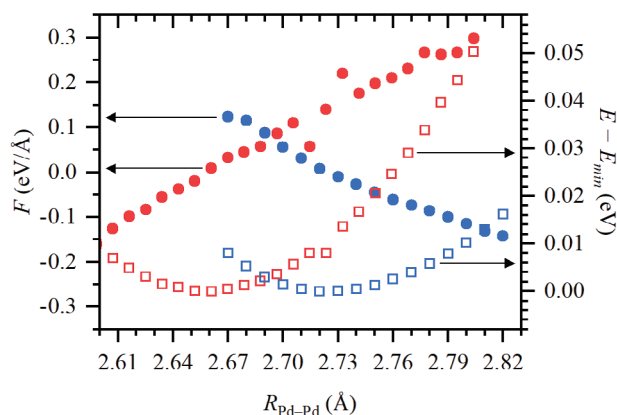
Figure 9. Energy profiles per one Pd atom in the unit cell (hollow squares, right ordinate axis) and their first derivatives (solid circles, left ordinate axis) calculated for Pd(100) (in blue) and PdO(101) (in red) surfaces as a function of cell parameters, recalculated into the first-shell Pd–Pd distances to present the data in a uniform way.

value of 2.74 ± 0.01 Å. The equilibrium cell parameter of PdO(101) would correspond to the Pd–Pd distance in metallic Pd of 2.659 Å. Therefore, the growth of the oxide layer on metallic Pd should cause the lattice contraction in the latter. In the case of an equal amount of Pd atoms in both phases, the predicted equilibrium Pd–Pd distance in metallic Pd is 2.69 Å (the intersection of red and blue circles in Figure 9. The predicted distance for interface with 25 Pd atoms in the metallic phase and 8 Pd atoms in the oxide is 2.71 Å, which was reproduced by direct calculation (Figure S9c, Supporting Information) resulting in the cell parameter of 2.709 Å. Therefore, the contraction of the Pd–Pd distances observed by time-resolved EXAFS is directly related to the alignment of the metallic and oxidic phases of palladium upon the restructuring of the palladium nanoparticles in the presence of molecular oxygen. It should be also noted, that, unlike the first-shell Pd–Pd distances which are rigidly linked with the Pd cell parameter, the Pd−O distances are not strictly linked to the cell parameters, which can explain why the experimental difference in the interatomic distances was observed only for Pd–Pd.

3. Conclusions

By a systematic time-resolved in situ investigation on a set of well-defined 2.3 nm palladium nanoparticles complemented by theoretical simulations we achieved a mechanistic understanding of palladium oxidation summarized in **Figure 10**: 1) A core@shell (Pd@PdO) type of structure is formed during the oxidation of metallic palladium nanoparticles by molecular oxygen. 2) At temperatures above 200 °C the oxide shell grows toward the bulk of the particle, forming a complete palladium oxide. 3) The oxidation starts from the low-coordinated Pd sites and weakens the metal-support interaction. 4) The local structure of Pd(II) species remains 4-coordinated irrespective of the temperature and particle size. 5) Formation of the PdO/Pd interface causes the contraction of Pd–Pd distances in the metallic core of the particles proportional to the fraction of the oxide phase.

4. Experimental Section

Materials: Commercial palladium catalysts, 5% Pd/Al$_2$O$_3$ and 4% Pd/P4VP, were supplied by Chimet S.p.A. The 5% Pd/Al$_2$O$_3$ catalyst was prepared using commercial high-surface-area transition alumina as the support (specific surface area, 116 m^2 g^{-1}; pore volume, 0.41 cm^3 g^{-1}) following a deposition-precipitation method using Na$_2$PdCl$_4$ as a metal precursor and Na$_2$CO$_3$ as the basic agent, as described elsewhere.[48] After Pd deposition, the catalyst was pre-reduced in aqueous solution using sodium formate at 65 °C for 1 h. The catalyst was carefully washed with water until complete removal of chlorine residues and dried overnight at 110 °C. The 5% Pd/Al$_2$O$_3$ sample has a palladium particle size of ≈2.3 ± 0.6 nm determined by HR-TEM and a dispersion of 38.1% determined by CO pulsed chemisorption method.[49]

The 4% Pd/P4VP catalyst was prepared by using Pd(II) acetate (hereafter Pd(OAc)$_2$) as a metal precursor and a poly-4-vinylpyridine 25% cross-linked with divinylbenzene (Sigma-Aldrich, hereafter P4VP), showing a specific surface area of ≈50 m^2 g^{-1} as support. P4VP (in the form of microspheres) was added to an orange solution of Pd(OAc)$_2$ in acetonitrile containing 4 wt.% of Pd with respect to the support and left under stirring at room temperature overnight. The solution appeared completely decolored, the sample was filtered, successively dried at room temperature, and mildly ground in an agate mortar. The average size of palladium particles in the sample after the activation procedure (*vide infra*) was ≈1.6 ± 0.3 nm.[15] Both samples have been objects of extensive characterization in the past.[49–52]

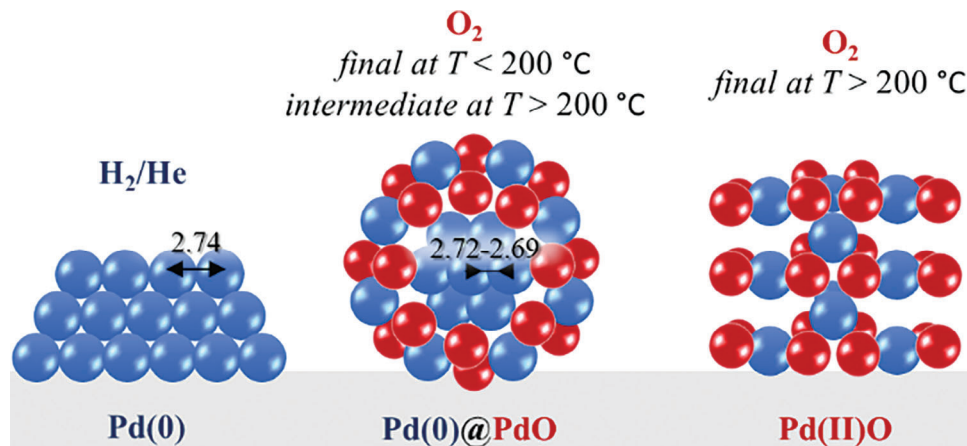**Figure 10.** A schematic summary of the oxidation of palladium nanoparticles.

ADVANCED
SCIENCE NEWS

www.advancedsciencenews.com

NANO · MICRO

small

www.small-journal.com

In Situ XAS Measurements and Data Analysis: In situ XAS data were collected at BM31 beamline[53] of ESRF (Grenoble, France). The catalyst powder was sieved to 116–200 µm and successively loaded into a 2 mm quartz capillary fixed from both sides by quartz wool. The capillary was glued into a metal sample holder connected to a remotely controlled gas panel permanently installed at BM31. The gas flows were remotely controlled by electronic mass flow controllers (Bronkhorst) and electro-valves. The temperature was regulated by the heat gun located below the sample and was monitored online by a thermocouple inserted directly inside the capillary and touching the catalyst powder. The outlet of the capillary was connected to the online mass spectrometer (Pfeiffer OmniStar GSD 320) to monitor the products (mainly, water) during the in situ procedure.

Once loaded into the capillary (quartz glass, 2 mm thickness), the fresh samples were flushed at room temperature by pure He (50 mL min^{-1}) for 15 min and then activated in 20%H_2/He flow for 30 min at 120 °C for Pd/Al$_2$O$_3$ and 1 h at 180 °C for Pd/P4VP to ensure pure metallic state of the particles. Time and temperature were optimized in our previous experiments.[49,50] The fully reduced samples will be referred to as Pd(0)/Al$_2$O$_3$ and Pd(0)/P4VP, respectively. After activation, the two catalysts were subjected to a sequence of oxidation and reduction cycles at increasing temperature from 50 to 400 °C. At each temperature the gasses were sent in the following order: 0) pure He, 1) 20% O$_2$/He to form the oxide phase, 2) pure He to remove gas phase oxygen, 3) 20% H$_2$/He to reduce Pd back to Pd(0). Since the full reduction to metallic Pd was observed in H$_2$ at each temperature after the corresponding oxidation step, no additional re-activation was performed in between the cycles. The Pd/Al$_2$O$_3$ sample after prolonged treatment in O$_2$ at 400 °C will be used as a reference for completely oxidized Pd nanoparticles and referred to as Pd(II)/Al$_2$O$_3$. Bulk palladium foil and commercial PdO sample (Acros Organics NV) were used as Pd(0) and Pd(II) standards.

XAS data were collected in situ during the above procedure. The signal was registered in transmission geometry using ionization chambers. The edge jump was ca. 0.4 and 0.2 for Pd/Al$_2$O$_3$ and Pd/P4VP samples, respectively. A third chamber was used for simultaneous measurement of Pd foil for energy calibration. The energy was scanned by a double crystal Si(111) monochromator operated in the continuous scanning mode (10 s per spectrum) in the 24.1–25.2 keV range. XAS spectra were processed in Python 3.7 using self-written procedures for data alignment, normalization, PyFitIt[54] and pyMCR libraries for principle component analysis (PCA) and multivariate curve resolution analysis[55] of XANES spectra, and Larch library[56,57] for EXAFS fitting. For the latter, two contributions, Pd-O and Pd-Pd, were used with variable interatomic distances (R), Debye-Waller parameters (σ^2), and zero energy shift (ΔE_0). The coordination number for Pd-O was fixed to 4, as expected for bulk PdO, while the Pd-Pd coordination number and relative fraction of metallic Pd and PdO phases were kept as variables. Each spectrum was fitted independently in the R-range of 1–3 Å (phase-uncorrected) using $k^{1,2,3}$-weighted data in the k-range of 3–12 Å^{-1}.

Molecular Dynamics and DFT Simulations: Molecular dynamics simulations with ReaxFF force-fields[58,59] were performed and visualized in AMS v.2021.1 software (SCM, Theoretical Chemistry, Vrije Universiteit, Amsterdam). A fcc-like cuboctahedron particle of 561 Pd atoms was placed in a cubic box with a = 10 nm and surrounded by 1000 oxygen molecules. The particle dimensions were 2.0 nm between the opposite (100) facets, 2.3 nm between the opposite (111) facets, and 2.8 between the opposite vertex atoms. The simulations were run at the constant temperature of 273, 473, and 673 K with Nosé-Hoover thermostats (damping constant 100 fs). The total simulation time was set to 1 ns, with the integration time of 0.25 fs. Prior to the visualization of the selected snapshots, the formed structures were relaxed with the same potential without gas phase molecules.

VASP[60–62] of Pd and PdO surfaces were performed with PBE functional. The cut-off energy for the plane-wave basis was set to 700 eV. The 8*8*1 Monkhorst–Pack grid was used to sample the k-space. The Pd(100) surface was created based on the *fcc* crystal structure with 5 layers of Pd atoms and a 10 Å vacuum layer in *z*-direction. The PdO(101) surface con-

tained 4 layers of Pd and O atoms and a 10 Å vacuum layer in *z*-direction. For the interface, the ($\sqrt{5}$x$\sqrt{5}$)R27° surface oxide on Pd(100) was considered. For every type of structure, a set of input geometries was generated by varying the x- and y- basis vectors of the unit cell, and geometry relaxation was performed for every value of x = y. These data were used to calculate the energy profiles as the function of cell parameter, which was recalculated into first shell Pd–Pd distance, and forces created upon cell deformation: for Pd(100) energy was scaled by a factor of 5 as the number of atoms in ($\sqrt{5}$x$\sqrt{5}$)R27 supercell was 5 times larger, and for PdO(101) the abscissa axis was divided by $\sqrt{5}$ after calculating the derivative of energy.

Statistical Analysis: The experimental XAS dataset consisted of more than 6000 spectra, which are made freely available at dx.doi.org/10.5281/zenodo.10657314. Each spectrum was analyzed independently using a procedure described in the Section 2.2. Reproducibility of the results was confirmed by repeating each experimental step twice on the same sample (the data in the Results and Discussion section correspond to the first runs at each temperature). The fitting of EXAFS data was performed in R-space by minimization of χ^2-function[63] calculated for the Fourier-transformed experimental and modelled $\chi(k)$. The number of maximal variable parameters was determined based on the fitting ranges in R- and k-spaces according to Nyquist criterion as N_{idp} = $2\Delta R\Delta k/\pi$. The standard error of the fitting parameters was determined in a standard way using Larch routine, based on the curvature of the χ^2-function, taking as the tolerance level the root-mean-square average of the high-R part of the $\chi(R)$ signal, where no structural contributions but rather random fluctuations are expected.[64]

Supporting Information

Supporting Information is available from the Wiley Online Library or from the author.

Conflict of Interest

The authors declare no conflict of interest.

Data Availability Statement

The data that support the findings of this study are openly available in [zenodo] at [https://doi.org/10.5281/zenodo.11426539], reference number [11426539].

Keywords

core-shell, EXAFS, palladium oxide, XANES

[1] D. Ciuparu, M. R. Lyubovsky, E. Altman, L. D. Pfefferle, A. Datye, *Catal. Rev.* 2002, *44*, 593.

ADVANCED
SCIENCE NEWS

www.advancedsciencenews.com

NANO · MICRO
small

www.small-journal.com

[2] J. Gustafson, O. Balmes, C. Zhang, M. Shipilin, A. Schaefer, B. Hagman, L. R. Merte, N. M. Martin, P.-A. Carlsson, M. Jankowski, E. J. Crumlin, E. Lundgren, *ACS Catal.* **2018**, *8*, 4438.

[3] Y. Zheng, L. Zhang, H. Jiang, C. Li, Y. Hu, *Small* **2024**, 2311346.

[4] J.-D. Grunwaldt, M. Caravati, A. Baiker, *J. Phys. Chem. B* **2006**, *110*, 25586.

[5] E. Groppo, A. Lazzarini, M. Carosso, A. Bugaev, M. Manzoli, R. Pellegrini, C. Lamberti, D. Banerjee, A. Longo, *ACS Catal.* **2018**, *8*, 6870.

[6] W. Wu, H. Jiang, *Accounts Chem. Res.* **2012**, *45*, 1736.

[7] S. Wang, D. E. Doronkin, M. Hahsler, X. Huang, D. Wang, J. D. Grunwaldt, S. Behrens, *ChemSusChem* **2020**, *13*, 3243.

[8] C. Chen, X. Wang, B. Pan, W. Xie, Q. Zhu, Y. Meng, Z. Hu, Q. Sun, *Small* **2023**, *19*, 2300114.

[9] T. Moragues, G. Giannakakis, A. Ruiz-Ferrando, C. N. Borca, T. Huthwelker, A. Bugaev, A. J. de Mello, J. Pérez-Ramírez, S. Mitchell, *Angew. Chem.* **2024**, 202401056.

[10] I. Beckers, C. Vos, H. Van Dessel, A. Lauwers, W. Stuyck, O. Usoltsev, A. Skorynina, A. Bugaev, D. De Vos, *ACS Catal.* **2024**, *14*, 7080.

[11] I. Beckers, A. Bugaev, D. De Vos, *Chem. Sci.* **2023**, *14*, 1176.

[12] J. Vercammen, M. Bocus, S. Neale, A. Bugaev, P. Tomkins, J. Hajek, S. Van Minnebruggen, A. Soldatov, A. Krajnc, G. Mali, *Nat. Catal.* **2020**, *3*, 1002.

[13] N. Van Velthoven, Y. Wang, H. Van Hees, M. Henrion, A. L. Bugaev, G. Gracy, K. Amro, A. V. Soldatov, J. G. Alauzun, P. H. Mutin, *ACS Appl. Mater. Interfaces* **2020**, *12*, 47457.

[14] J. D. Grunwaldt, M. Caravati, A. Baiker, *J. Phys. Chem. B* **2006**, *110*, 25586.

[15] E. Groppo, A. Lazzarini, M. Carosso, A. Bugaev, M. Manzoli, R. Pellegrini, C. Lamberti, D. Banerjee, A. Longo, *ACS Catal.* **2018**, *8*, 6870.

[16] J.-D. Grunwaldt, N. van Vegten, A. Baiker, *Chem. Commun.* **2007**, 4635.

[17] R. Burch, F. J. Urbano, *Appl. Catal. A* **1995**, *124*, 121.

[18] S. C. Su, J. N. Carstens, A. T. Bell, *J. Catal.* **1998**, *176*, 125.

[19] C. T. Campbell, D. C. Foyt, J. M. White, *J. Phys. Chem.* **2002**, *81*, 491.

[20] B. Brandt, T. Schalow, M. Laurin, S. Schauermann, J. Libuda, H. J. Freund, *J. Phys. Chem. C* **2006**, *111*, 938.

[21] X. Li, X. Wang, K. Roy, J. A. van Bokhoven, L. Artiglia, *ACS Catal.* **2020**, *10*, 5783.

[22] A. L. Bugaev, A. A. Guda, A. Lazzarini, K. A. Lomachenko, E. Groppo, R. Pellegrini, A. Piovano, H. Emerich, A. V. Soldatov, L. A. Bugaev, V. P. Dmitriev, J. A. van Bokhoven, C. Lamberti, *Catal. Today* **2017**, *283*, 119.

[23] A. V. Dobrovolskaya, S. V. Chapek, O. A. Usoltsev, E. Naranov, D. N. Gorbunov, A. L. Trigub, A. L. Maximov, A. V. Soldatov, A. L. Bugaev, *J. Phys. Chem. C* **2023**, *127*, 20727.

[24] A. Ramirez, P. Ticali, D. Salusso, T. Cordero-Lanzac, S. Ould-Chikh, C. Ahoba-Sam, A. L. Bugaev, E. Borfecchia, S. Morandi, M. Signorile, S. Bordiga, J. Gascon, U. Olsbye, *JACS Au* **2021**, *1*, 1719.

[25] S. K. Matam, G. L. Chiarello, Y. Lu, A. Weidenkaff, D. Ferri, *Top. Catal.* **2013**, *56*, 239.

[26] S. K. Matam, M. H. Aguirre, A. Weidenkaff, D. Ferri, *J. Phys. Chem. C* **2010**, *114*, 9439.

[27] A. W. Petrov, D. Ferri, F. Krumeich, M. Nachtegaal, J. A. van Bokhoven, O. Krocher, *Nat. Commun.* **2018**, *9*, 2545.

[28] P. Lott, P. Dolcet, M. Casapu, J.-D. Grunwaldt, O. Deutschmann, *Ind. Eng. Chem. Res.* **2019**, *58*, 12561.

[29] P. Velin, F. Hemmingsson, A. Schaefer, M. Skoglundh, K. A. Lomachenko, A. Raj, D. Thompsett, G. Smedler, P. A. Carlsson, *ChemCatChem* **2021**, *13*, 3765.

[30] T. Fovanna, I. Alxneit, A. H. Clark, S. Checchia, M. Di Michiel, O. Kröcher, M. Nachtegaal, D. Ferri, *J. Phys. Chem. C* **2021**, *125*, 16473.

[31] J. Stötzel, R. Frahm, B. Kimmerle, M. Nachtegaal, J.-D. Grunwaldt, *J. Phys. Chem. C* **2011**, *116*, 599.

[32] T. Li, A. Beck, F. Krumeich, L. Artiglia, M. K. Ghosalya, M. Roger, D. Ferri, O. Kröcher, V. Sushkevich, O. V. Safonova, J. A. van Bokhoven, *ACS Catal.* **2021**, *11*, 7371.

[33] O. A. Usoltsev, A. A. Skorynina, B. O. Protsenko, V. Martin-Diaconescu, R. Pellegrini, A. V. Soldatov, J. van Bokhoven, A. L. Bugaev, *Appl. Surf. Sci.* **2023**, *614*, 156171.

[34] A. L. Bugaev, A. A. Guda, K. A. Lomachenko, V. V. Shapovalov, A. Lazzarini, J. G. Vitillo, L. A. Bugaev, E. Groppo, R. Pellegrini, A. V. Soldatov, J. A. van Bokhoven, C. Lamberti, *J. Phys. Chem. C* **2017**, *121*, 18202.

[35] A. L. Bugaev, A. A. Guda, K. A. Lomachenko, V. V. Srabionyan, L. A. Bugaev, A. V. Soldatov, C. Lamberti, V. P. Dmitriev, J. A. van Bokhoven, *J. Phys. Chem. C* **2014**, *118*, 10416.

[36] A. L. Bugaev, A. A. Guda, K. A. Lomachenko, A. Lazzarini, V. V. Srabionyan, J. G. Vitillo, A. Piovano, E. Groppo, L. A. Bugaev, A. V. Soldatov, V. P. Dmitriev, R. Pellegrini, J. A. van Bokhoven, C. Lamberti, *J. Phys. Conf. Ser.* **2016**, *712*, 012032.

[37] A. L. Bugaev, A. A. Guda, K. A. Lomachenko, E. G. Kamyshova, M. A. Soldatov, G. Kaur, S. Øien-Ødegaard, L. Braglia, A. Lazzarini, M. Manzoli, S. Bordiga, U. Olsbye, K. P. Lillerud, A. V. Soldatov, C. Lamberti, *Faraday Discuss.* **2018**, *208*, 287.

[38] O. Usoltsev, A. Tereshchenko, A. Skorynina, E. Kozyr, A. Soldatov, O. Safonova, A. H. Clark, M. Nachtegaal, A. Bugaev, *Small Methods* **2024**, 2301397.

[39] A. A. Skorynina, A. Lazzarini, D. K. Sannes, E. G. Kozyr, C. Ahoba-Sam, S. Bordiga, U. Olsbye, A. L. Bugaev, *J. Mater. Chem. C* **2024**, *12*, 3564.

[40] A. L. Bugaev, O. A. Usoltsev, A. A. Guda, K. A. Lomachenko, I. A. Pankin, Y. V. Rusalev, H. Emerich, E. Groppo, R. Pellegrini, A. V. Soldatov, J. A. van Bokhoven, C. Lamberti, *J. Phys. Chem. C* **2018**, *122*, 12029.

[41] A. L. Bugaev, O. A. Usoltsev, A. Lazzarini, K. A. Lomachenko, A. A. Guda, R. Pellegrini, M. Carosso, J. G. Vitillo, E. Groppo, J. A. van Bokhoven, A. V. Soldatov, C. Lamberti, *Faraday Discuss.* **2018**, *208*, 187.

[42] A. L. Bugaev, A. A. Guda, I. A. Pankin, E. Groppo, R. Pellegrini, A. Longo, A. V. Soldatov, C. Lamberti, *Catal. Today* **2019**, *336*, 40.

[43] A. A. Skorynina, A. A. Tereshchenko, O. A. Usoltsev, A. L. Bugaev, K. A. Lomachenko, A. A. Guda, E. Groppo, R. Pellegrini, C. Lamberti, A. Soldatov, *Radiat. Phys. Chem.* **2020**, *175*, 108079.

[44] O. A. Usoltsev, A. Y. Pnevskaya, E. G. Kamyshova, A. A. Tereshchenko, A. A. Skorynina, W. Zhang, A. L. Bugaev, A. V. Soldatov, *Nanomaterials* **2020**, *10*, 1643.

[45] A. L. Bugaev, O. A. Usoltsev, A. A. Guda, K. A. Lomachenko, M. Brunelli, E. Groppo, R. Pellegrini, A. V. Soldatov, J. van Bokhoven, *Faraday Discuss.* **2021**, *229*, 197.

[46] O. A. Usoltsev, A. L. Bugaev, A. A. Guda, S. A. Guda, A. V. Soldatov, *Top. Catal.* **2020**, *63*, 58.

[47] A. L. Bugaev, M. Zabilskiy, A. A. Skorynina, O. A. Usoltsev, A. V. Soldatov, J. A. van Bokhoven, *Chem. Commun.* **2020**, *56*, 13097.

[48] G. Agostini, E. Groppo, A. Piovano, R. Pellegrini, G. Leofanti, C. Lamberti, *Langmuir* **2010**, *26*, 11204.

[49] E. Groppo, G. Agostini, A. Piovano, N. B. Muddada, G. Leofanti, R. Pellegrini, G. Portale, A. Longo, C. Lamberti, *J. Catal.* **2012**, *287*, 44.

[50] E. Groppo, W. Liu, O. Zavorotynska, G. Agostini, G. Spoto, S. Bordiga, C. Lamberti, A. Zecchina, *Chem. Mater.* **2010**, *22*, 2297.

[51] M. Carosso, E. Vottero, S. Morandi, M. Manzoli, D. Ferri, T. Fovanna, R. Pellegrini, A. Piovano, E. Groppo, *ChemCatChem* **2020**, *13*, 900.

[52] A. Lazzarini, E. Groppo, G. Agostini, E. Borfecchia, F. Giannici, G. Portale, A. Longo, R. Pellegrini, C. Lamberti, *Catal. Today* **2017**, *283*, 144.

[53] W. van Beek, O. V. Safonova, G. Wiker, H. Emerich, *Phase Transit.* **2011**, *84*, 726.

[54] A. Martini, S. A. Guda, A. A. Guda, G. Smolentsev, A. Algasov, M. A. Soldatov, A. Bugaev, Y. Rusalev, C. Lamberti, A. V. Soldatov, *Comput. Phys. Commun* **2020**, *250*, 107064.

[55] C. H. Camp, *J. Res. Natl. Inst. Stand. Technol.* **2019**, *124*.

[56] M. Newville, *J. Phys. Conf. Ser.* **2013**, *430*, 012007.

[57] B. Ravel, M. Newville, *J. Synchrot. Radiat.* **2005**, *12*, 537.

[58] A. C. T. van Duin, S. Dasgupta, F. Lorant, W. A. Goddard, *J. Phys. Chem. A* **2001**, *105*, 9396.

[59] K. Chenoweth, A. C. van Duin, W. A. Goddard, *J. Phys. Chem. A* **2008**, *112*, 1040.

[60] G. Kresse, J. Furthmüller, *Phys. Rev. B* **1996**, *54*, 11169.

[61] G. Kresse, D. Joubert, *Phys. Rev. B* **1999**, *59*, 1758.

[62] J. Hafner, *J. Comput. Chem.* **2008**, *29*, 2044.

[63] P. R. Bevington, D. K. Robinson, McGraw—Hill, New York **2003**.

[64] B. Boyanov, M. Newville, D. Sayers, *Synchrotron Radiation* **1999**, *6*, 521.

[65] R. F. Pettifer, O. Mathon, S. Pascarelli, M. D. Cooke, M. R. Gibbs, *Nature* **2005**, *435*, 78.

[66] J. D. Grunwaldt, N. van Vegten, A. Baiker, *Chem. Commun.* **2007**, 4635.

[67] M. Todorova, E. Lundgren, V. Blum, A. Mikkelsen, S. Gray, J. Gustafson, M. Borg, J. Rogal, K. Reuter, J. N. Andersen, M. Scheffler, *Surf. Sci.* **2003**, *541*, 101.